Photoluminescence at the ground-state level anticrossing of the nitrogen-vacancy center in diamond: A comprehensive study

Viktor Ivády [1,2,*] Huijie Zheng,[3,4,†] Arne Wickenbrock,[3,4] Lykourgos Bougas [3] Georgios Chatzidrosos,[3]
Kazuo Nakamura [5] Hitoshi Sumiya [6] Takeshi Ohshima [7] Junichi Isoya,[8]
Dmitry Budker [3,4,9] Igor A. Abrikosov [2] and Adam Gali [1,10]

[1]*Wigner Research Centre for Physics, PO Box 49, H-1525, Budapest, Hungary*
[2]*Department of Physics, Chemistry and Biology, Linköping University, SE-581 83 Linköping, Sweden*
[3]*Johannes Gutenberg-Universität Mainz, 55128 Mainz, Germany*
[4]*Helmholtz-Institut, GSI Helmholtzzentrum für Schwerionenforschung, 55128 Mainz, Germany*
[5]*Leading-Edge Energy System Research Institute, Fundamental Technology Dept., Tokyo Gas Co., Ltd., Yokohama, 230-0045 Japan*
[6]*Advanced Materials Laboratory, Sumitomo Electric Industries, Ltd., Itami, 664-0016 Japan*
[7]*Takasaki Advanced Radiation Research Institute, National Institutes for Quantum and Radiological Science and Technology,
Takasaki, 370-1292, Japan*
[8]*Faculty of Pure and Applied Sciences, University of Tsukuba, Tsukuba, 305-8573 Japan*
[9]*Department of Physics, University of California, Berkeley, California 94720-7300, USA*
[10]*Department of Atomic Physics, Budapest University of Technology and Economics, Budafoki út 8., H-1111 Budapest, Hungary*

The nitrogen-vacancy center (NV center) in diamond at magnetic fields corresponding to the ground-state level anticrossing (GSLAC) region gives rise to rich photoluminescence (PL) signals due to the vanishing energy gap between the electron spin states, which enables for a broad variety of environmental couplings to have an effect on the NV center's luminescence. Previous works have addressed several aspects of the GSLAC photoluminescence, however, a comprehensive analysis of the GSLAC signature of NV ensembles in different spin environments at various external fields is missing. Here we employ a combination of experiments and recently developed numerical methods to investigate in detail the effects of transverse electric and magnetic fields, strain, P1 centers, NV centers, and the ^{13}C nuclear spins on the GSLAC photoluminescence. Our comprehensive analysis provides a solid ground for advancing various microwave-free applications at the GSLAC, including but not limited to magnetometry, spectroscopy, dynamic nuclear polarization (DNP), and nuclear magnetic resonance (NMR) detection. We demonstrate that not only the most abundant ^{14}NV center but the ^{15}NV can also be utilized in such applications.

I. INTRODUCTION

Over the last decade, the NV center in diamond [1–4] has demonstrated considerable potential in spectroscopy and sensing applications [5–9]. The NV center exhibits a level anticrossing in the electronic ground state (GSLAC) at magnetic field $B_z = \pm 102.4$ mT, which has been recently exploited in microwave-free applications, ranging from magnetometry [10–12] through nuclear-magnetic-resonance spectroscopy [10,13–15] to optical hyperpolarization [16–18]. These applications are of special interest in biology and medicine, where high-power microwave driving is undesirable.

The physics of isolated NV centers at the GSLAC is well understood [10,17,19], however, the effects of environmental perturbations are not comprehensively described. Due to the presence of ^{14}N (^{15}N) nuclear spin, six (four) mixed electron-nuclear spin states either cross or exhibit an avoided crossing. External perturbations and interaction with the local nuclear and electron spin environment may give rise to additional spin-relaxation mechanisms at specific magnetic fields corresponding to the crossings of the spin states. Through the spin-dependent PL of the NV center, these processes may give rise to various PL signals at the GSLAC [12,20–22]. Besides the optical signal, optically detected magnetic resonance (ODMR) signal of a NV ensemble has been recently recorded [23]. Recently, the ground-state level anticrossing at zero magnetic field and related phenomena have attracted considerable attention [24,25]. As increasing number of applications rely on LAC signals of single or ensemble NV systems, quantitative description of the most relevant environmental couplings is essential for further development and engineering of these applications.

---

*Corresponding author: ivady.viktor@wigner.hu
†Corresponding author: zheng@uni-mainz.de

Furthermore, interaction between NV centers and ^{13}C nuclear spins at the GSLAC can potentially be utilized in dynamic nuclear polarization (DNP) [26–28] applications. DNP can give rise to a hyperpolarized diamond sample with a potential to transfer spin polarization to adjacent nuclear spins for the improvement of traditional nuclear magnetic resonance methods [16,18,29–33]. It is therefore of fundamental importance to gain detailed insight into the NV-^{13}C spin dynamics at the GSLAC.

In this paper we aim at establishing a guideline for developing and advancing applications at the GSLAC of the NV center in diamond by collecting and describing the most relevant interactions that may either limit existing applications or give rise to new ones. Indeed, by identifying the PL signals of different environmental couplings we reveal important interactions that enable new spectroscopy, magnetometry, and DNP applications.

To this end, we carry out a joint experimental and theoretical study, where we employ a quantum dynamic simulation technique, developed in Ref. [34]. This approach allows us to gain deep insight into the underlying physics of the GSLAC phenomena. The utilized theoretical approach describes spin flip-flop interactions of a spin ensemble in a spin conserving manner, thus it is an appropriate tool for studying spin mixing and spin relaxation which in turn give rise to PL signatures at the GSLAC.

The rest of the paper is organized as follows: In Sec. II we provide a brief overview of the established physics of the NV center. In Sec. III, we describe our experimental setup and samples and the details of the theoretical simulations. Section IV describes our results in four sections considering interactions of NV centers with external fields, ^{13}C nuclear spins, P1 centers, and other NV centers at the GSLAC. Finally, in Sec. V, we summarize and discuss our results.

II. BACKGROUND

The NV center in diamond gives rise to a coupled hybrid register that consists of a spin-1 electron spin and either a spin-1 ^{14}N or spin-1/2 ^{15}N. Hereinafter, we refer to the former as ^{14}NV center and to the latter, less abundant configuration, as ^{15}NV center.

The spin Hamiltonian of the ^{14}NV center can be written as

$$H_{^{14}\text{N}} = D\left(S_z^2 - \frac{2}{3}\right) + g_e\beta\vec{S}\vec{B} + \vec{S}\mathcal{A}_{^{14}\text{N}}\vec{I}_{^{14}\text{N}}$$
$$+ Q\left(I_{^{14}\text{N},z}^2 - \frac{2}{3}\right) - g_{^{14}\text{N}}\beta_{\text{N}}\vec{I}_{^{14}\text{N}}\vec{B}, \quad (1)$$

where terms on the right-hand side describe zero-field splitting, Zeeman, hyperfine, nuclear quadrupole, and nuclear Zeeman interaction, respectively, $\vec{S}$ and $\vec{I}_{^{14}\text{N}}$ are the electron and nuclear spin operator vectors, and S_z and $I_{^{14}\text{N},z}$ are the electron and nuclear spin z operators, where the quantization axis z is parallel to the N-V axis. g_e and $g_{^{14}\text{N}}$ are the electron and ^{14}N nuclear g factors, β and β_{N} are the Bohr and nuclear magnetons, respectively, $\vec{B}$ is the external magnetic field, $D = 2868.91$ MHz is the zero-field splitting, $Q = -5.01$ MHz [35] is the nuclear quadrupole splitting, and $\mathcal{A}^{^{14}\text{N}}$ is the hyperfine tensor of the ^{14}N nuclear spin that can be expressed by its diagonal elements $A_{xx} = A_{yy} = A_\perp = -2.70$ MHz and $A_{zz} = A_\parallel = -2.14$ MHz [35]. The spin Hamiltonian of the ^{15}NV

center can be written as

$$H_{^{15}\text{N}} = D\left(S_z^2 - \frac{2}{3}\right) + g_e\beta\vec{S}\vec{B} + \vec{S}\mathcal{A}_{^{15}\text{N}}\vec{I}_{^{15}\text{N}} - g_{^{15}\text{N}}\beta_{\text{N}}\vec{I}_{^{15}\text{N}}\vec{B}, \quad (2)$$

where $g_{^{15}\text{N}}$ is the nuclear g factor of ^{15}N nucleus, and $\mathcal{A}_{^{15}\text{N}}$ is the hyperfine tensor of the ^{15}N nuclear spin that can be expressed by its nonzero diagonal elements $A_\perp = +3.65$ MHz and $A_\parallel = +3.03$ MHz [35].

Diamond contains 1.07% spin-1/2 ^{13}C isotope in natural abundance that can effectively interact with the NV electron spin at the GSLAC through the hyperfine interaction. The Hamiltonian of a ^{13}C nuclear spin coupled to a NV center can be written as

$$H_{^{13}\text{C}} = g_{^{13}\text{C}}\mu_N\vec{B}\vec{I}_{^{13}\text{C}} + \vec{S}A_{^{13}\text{C}}\vec{I}_{^{13}\text{C}}, \quad (3)$$

where $\vec{I}_{^{13}\text{C}}$ is the nuclear spin operator vector, $g_{^{13}\text{C}}$ is the nuclear g factor of ^{13}C nucleus, and $A_{^{13}\text{C}}$ is the hyperfine tensor that consists of two terms, the isotropic Fermi contact term and the anisotropic dipolar interaction term,

$$A_{^{13}\text{C}} = A_{^{13}\text{C}}^{\text{Fc}} + A_{^{13}\text{C}}^{\text{d}}. \quad (4)$$

Due to the typically low symmetry of the NV-^{13}C coupling, all six independent elements of the hyperfine tensor can be nonzero in the coordinate system of the NV center. These components can be expressed by the diagonal hyperfine tensor elements, $A_{xx} \approx A_{yy} = A_\perp$ and $A_{zz} = A_\parallel$, as well as angle θ of the principal hyperfine axis $\mathbf{e}_z$ and the symmetry axis of the NV center. The hyperfine Hamiltonian, expressed in the basis of $|m_S, m_{^{13}\text{C}}\rangle = \{|0,\uparrow\rangle, |0,\downarrow\rangle, |-1,\uparrow\rangle, |-1,\downarrow\rangle\}$, can be written as

$$H_{^{13}\text{C}} = \vec{S}A_{^{13}\text{C}}\vec{I}_{^{13}\text{C}} = \frac{1}{2}\begin{pmatrix} 0 & 0 & \frac{1}{\sqrt{2}}b & \frac{1}{\sqrt{2}}c_- \\ 0 & 0 & \frac{1}{\sqrt{2}}c_+ & -\frac{1}{\sqrt{2}}b \\ \frac{1}{\sqrt{2}}b & \frac{1}{\sqrt{2}}c_+ & -A_z & -b \\ \frac{1}{\sqrt{2}}c_- & -\frac{1}{\sqrt{2}}b & -b & A_z \end{pmatrix},$$
$$(5)$$

where

$$A_z = A_\parallel \cos^2\theta + A_\perp \sin^2\theta, \quad (6)$$

$$b = (A_\parallel - A_\perp)\cos\theta\sin\theta, \quad (7)$$

$$c_\pm = A_\parallel \sin^2\theta + A_\perp(\cos^2\theta \pm 1). \quad (8)$$

Parameters A_z and b of the hyperfine Hamiltonian describe effective longitudinal and transverse magnetic fields due to the interaction with the ^{13}C nuclear spin, respectively, while parameters c_+ and c_- are responsible for mutual spin flip flops of the ^{13}C nuclear spin and the NV center. Note that there are nonzero matrix elements that correspond, for example, to $S_+ I_+^{^{13}C}$ or $S_+ I_z^{^{13}C}$ operator combinations. The appearance of such terms implies that m_S and $m_{^{13}\text{C}}$ are no longer good quantum numbers.

Besides nuclear spins, the NV center can interact with other spin defects, such as the spin-1/2 nitrogen substitution point defect (P1 center) and other NV centers. The spin Hamiltonian

of the P1 center can be written as

$$H_{P1} = g_e\beta\vec{S}^{P1}\vec{B} + \vec{S}^{P1}\mathcal{A}_{z'}^{P1}\vec{I}^{P1} + Q_{z'}^{P1}\left(\left(I_{z'}^{P1}\right)^2 - \tfrac{2}{3}\right)$$
$$- g_N\beta_N\vec{I}_{z'}^{P1}\vec{B}, \tag{9}$$

where $\mathcal{A}^{P1}$ is the hyperfine interaction tensor that can be expressed by $A_\perp^{P1} = 81$ MHz and $A_\parallel^{P1} = 114$ MHz diagonal elements. For simplicity the quadrupole interaction strength is set to the value of the NV centers quadrupole splitting in this article, i.e., $Q^{P1} = -5.01$ MHz, which is comparable with the measured quadrupole splitting of -3.974 MHz of the P1 center [36]. As hyperfine interaction is dominating over the quadrupole splitting, the small deviation in the latter has negligible effect on the results. Both the P1 center and other NV centers may exhibit a distinct local quantization axis depending on the C_{3v} reconstruction and the N-V axis, respectively. We denote the symmetry and quantization axis of the P1 center in Eq. (9) by z'. The angle between z' and the quantization axis of the central NV center can be either $0°$ or $109.5°$. The spin Hamiltonian of NV center that has z' orientation can be obtained from Eq. (1) by a proper transformation of the coordinate system.

The interaction Hamiltonian between paramagnetic defects and the central NV center can be written as

$$H_J = \vec{S}\mathcal{J}\vec{S}^{\text{def}}, \tag{10}$$

where $\vec{S}^{\text{def}}$ is the spin operator vector of the spin defect and $\mathcal{J}$ is the coupling tensor. Assuming pointlike electron spin densities, $\mathcal{J}$ can be approximated by the dipole-dipole coupling tensor.

III. METHODOLOGY

A. Theoretical approaches

We employ two different theoretical approaches to study the GSLAC photoluminescence signal of NV ensembles interacting with external fields and environmental spins. For external fields, the density matrix ϱ of a single NV center is propagated over a finite time interval according to the master equation of the closed system,

$$\dot{\varrho} = -\frac{i}{\hbar}[H, \varrho], \tag{11}$$

where H is the ground-state spin Hamiltonian specified in Sec. II. The starting density matrix ϱ_0 is set to describe 100% polarization in the $|m_S, m_{^{14}N}\rangle = |0, +1\rangle$ state of the electron and the ^{14}N nuclear spins of the NV center. The PL intensity $\mathcal{I}$ is approximated from the time averaged density matrix according to the formula of

$$\mathcal{I} \approx \langle p_0 \rangle + (1 - C)\langle p_{\pm 1} \rangle, \tag{12}$$

where $\langle p_0 \rangle$ and $\langle p_{\pm 1} \rangle$ are the time averaged probabilities of finding the electron spin in $m_S = 0$ and $m_S = \pm 1$, respectively, and $C = 0.3$ is a reasonably experimentally attainable ODMR contrast.

To study the effects of environmental spins on the GSLAC photoluminescence signal, we apply a recently developed extended Lindblad formalism [34]. In this approach spin relaxation of a selected point defect surrounded by a bath of

environmental spins can be simulated over either a fixed simulation time or cycles of ground-state time evolution and optical excitation steps. The modeled systems consist of a central NV center, either ^{14}NV or ^{15}NV, and a bath of coupled environmental spins of the same kind. Different bath spins considered in our study are spin-1/2 ^{13}C, spin-1/2 P1 center with a spin-1 ^{14}N nuclear spin, and spin-1 ^{14}NV and ^{15}NV centers. To create a realistic spin bath, spin defects are distributed randomly in the diamond lattice around the central NV center in a sphere. To obtain ensemble averaged PL spectra, in all cases, we consider an ensemble of configurations, i.e., a set of random distributions of the spin defects. While each configuration describes a different local environment of the NV center, the ensembles describe a certain spin bath concentration on average. As a main approximation of the method, the many-spin system is divided into a cluster of subsystems. The number of spins included in each cluster determine the order of the cluster approximation. In the first-order cluster approximation no entanglement between the bath spins is taken into account. Higher order modeling allows inclusion of intra-spin-bath entanglement. For further details on the methodology see Ref. [34]. For simplicity, the mean field of the spin bath [34] is neglected in this study.

In the case of a ^{13}C spin bath, the nuclear spin-relaxation time is long compared to the inverse of the optical pump rate, which enables nuclear spin polarization to play a considerable role in the GSLAC PL signal of NV centers. Therefore, to simulate the PL signal we simulated a sequence of optical excitation cycles. Each of them included two steps, (1) coherent time evolution in the ground state with a dwell time t_{GS} set to 3 μs, and (2) spin selective optical excited process taken into account by a projection operator defined as

$$D = (1 - C)I + Cp_\pm P_{\pm 1 \to 0} + Cp_0 P_{0 \to 0}, \tag{13}$$

where I is the identity operator, $P_{i \to f}$ is a projector operator from $|m_S = i\rangle$ state to $|m_S = f\rangle$ state of the NV spin, and p_s is the probability of finding the system in state $|m_S = s\rangle$ ($s = 0, \pm 1$). Hyperfine coupling tensors between the central NV center and the nuclear spin are determined from first principles density function theory (DFT) calculations as specified in Refs. [34,37]. Spin relaxation in the excited state is neglected in this study. Typically 32 cycles are considered, which corresponds to ≈ 0.1 ms overall simulations time. We note that simulation of longer pumping is possible, however, beyond 0.1 ms we experience considerable finite-size effects in our model consisting of 127 nuclear spins, find more details in the Appendix. Based on the convergence tests summarized in the Appendix, we set the order parameter to 2, meaning that ^{13}C–^{13}C coupling is included in the model between pairs of close nuclear spins, and considered an ensemble of 100 random spin configurations in all cases when ^{13}C nuclear spin bath is considered.

For point-defect spin environments we make an assumption that the spin-relaxation time of the spin defects is shorter than the inverse of the coupling strength and the pump rate, thus dynamical polarization of the spin defects due to interaction with the central NV center may be neglected. Omitting optical polarization cycles, we simulate a ground-state time evolution of 0.1 ms dwell time to model such systems. For P1 center and NV center spin environments we assume

TABLE I. Specifications of the samples used in our experiments.

Sample	NV	P1	^{13}C
W4	10–20 ppb	1 ppm	1.07%
IS	0.9 ppm	2 ppm	0.03%
E6	2.3 ppm	13.8 ppm	0.01%
F11	<20 ppm	<200 ppm	1.07%

nonpolarized and nearly completely polarized states for the spin bath, respectively. Coupling tensors between the central and environmental spin are calculated from the dipole-dipole interaction Hamiltonian. Our ensembles induce 100 random spin defect configurations, each of them consisting of 127 spin defects. Electron spin defects usually possess shorter coherence time than the inverse of the NV coupling strength, therefore, the bath may be considered uncorrelated and the first-order cluster approximation is appropriate in these cases [34].

B. Samples and experimental methods

In our experiments we study different diamond samples with different defect concentration and ^{13}C abundance. Table I summarizes the most relevant properties of all the studied samples.

We carry out photoluminescence measurements on our samples. The experimental apparatus includes a custom-built electromagnet which provides magnetic field of 0 to about 110 mT. The electromagnet can be moved with a computer-controlled 3D translation stage and a rotation stage. The NV-diamond sensor is placed in the center of the magnetic bore. The diamond can be rotated around the z axis (along the direction of the magnetic field).

IV. RESULTS

In the following four sections we investigate experimentally and theoretically the most relevant interactions that can have significant effects on the GSLAC PL spectrum.

A. External fields

At the GSLAC region the parallel magnetic field is set so that $g_e\beta S_z B_z \approx D$. Due to the large splitting, $2D \approx 5.8$ GHz, between $m_S = +1$ level and the other electron spin levels and also the dominant spin polarization in the $m_S = 0$ spin state, the $m_S = +1$ level can be neglected. The relevant energy levels in the vicinity of the GSLAC are depicted in Fig. 1(a). The corresponding wave functions, expressed in the $|S_z, I_z\rangle$ basis, are provided in Table II. Besides the hyperfine interaction induced avoided crossings between levels γ and ε and β and ζ, one can identify seven crossings.

In the absence of external field and other spin defects in the environment, the GSLAC PL signal is a straight line with no fine structures at the GSLAC, as the ^{14}N hyperfine interaction does not allow further mixing of the highly polarized α state. External fields, however, give rise to additional spin flip-flop processes that open gaps at the crossings, mix the bright $m_S = 0$ and the dark $m_S = -1$ spin state, and thus imply fine
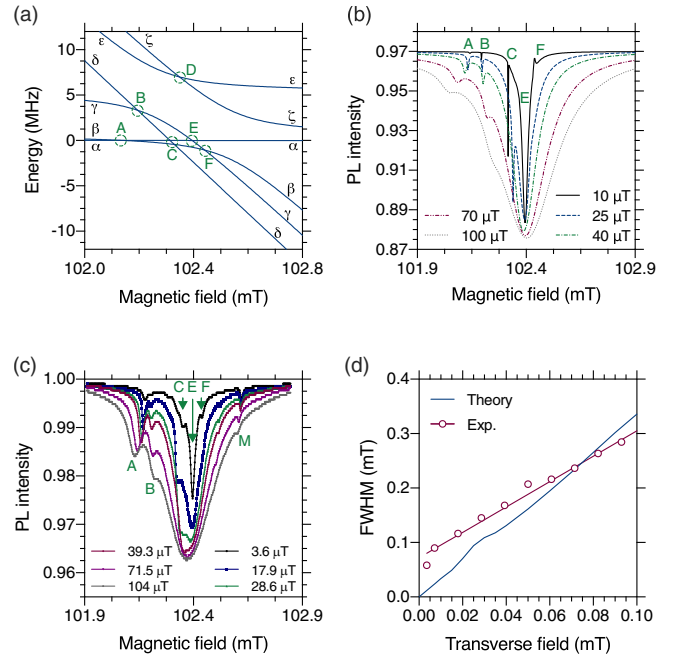

FIG. 1. (a) Energy level diagram of the ^{14}NV center. Greek letters denote the spin eigenenergies and green dashed circles with capital letters denote crossings where external perturbations may open gaps. (b) Theoretical PL signal vs longitudinal magnetic field at the GSLAC with different values of transverse magnetic field. (c) Experimental PL signal obtained from sample IS vs longitudinal magnetic field at the GSLAC with different values of transverse magnetic field. (d) Transverse magnetic field dependence of the full width at half maximum of the central dip E. Maroon open circles, maroon solid line, and blue solid line depict the experimental points, a linear fit, and the theoretical results, respectively.

structures in the GSLAC PL spectrum. In Table III we list spin flip-flop processes that may take place at crossing A–F, also labeled by two Greek letters that refer to the crossing states. We note that except for the $\alpha\delta$ crossing, all crossings allow additional spin mixing. Precession of the electron and ^{14}N nuclear spin may be induced by external transverse field. Cross relaxation between the electron and nuclear spin can happen when the initial, near unity polarization of the α state is reduced by external perturbations.

As 2×2 Pauli matrices, σ_x, σ_y, and σ_z, and the 2×2 identity matrix σ_0 span the space of 2×2 matrices, the spin

TABLE II. Energy eigenstates of the ^{14}NV center at the GSLAC as expressed in the basis of $|S_z, I_z\rangle$, where z is parallel to the N-V axis. a, b, c, and d are coefficients.

Label	Eigenstate
α	$\|0, +1\rangle$
β	$a\|0, -1\rangle + b\| -1, 0\rangle$
γ	$c\|0, 0\rangle + d\| -1, +1\rangle$
δ	$\| -1, -1\rangle$
ε	$c\| -1, +1\rangle - d\|0, 0\rangle$
ζ	$a\| -1, 0\rangle - b\|0, -1\rangle$

TABLE III. Characteristics of the level crossings at the GSLAC of the ^{14}NV. $(\Delta S, \Delta I)$ specifies spin flip-flop processes that may take place at the crossings.

Crossing		Spin state transitions	
		$(\Delta S, \Delta I)$	Remark
A	$\alpha\beta$	$(\pm 1, \mp 1)$	cross relaxation
B	$\gamma\delta$	$(\pm 1, \pm 1)$	cross relaxation
C	$\alpha\delta$		no spin state transition allowed
C'	$\beta\delta$	$(\pm 1, 0)$ and $(0, \pm 1)$	electron and ^{14}N spin precession
D	$\epsilon\zeta$	$(\pm 1, 0)$ and $(0, \pm 1)$	electron and ^{14}N spin precession
E	$\alpha\gamma$	$(\pm 1, 0)$ and $(0, \pm 1)$	electron and ^{14}N spin precession
F	$\beta\gamma$	$(\pm 1, 0)$ and $(0, \pm 1)$	electron and ^{14}N spin precession

Hamiltonian of any external field acting on the reduced two-dimensional basis of the NV electron spin can be expressed by the linear combination of these matrices at the GSLAC, as

$$\Delta H = \delta_x \sigma_x + \delta_y \sigma_y + \delta_z \sigma_z + \delta_0 \sigma_0. \quad (14)$$

This means that any time independent external perturbation acting on the electron spin of the NV center at the GSLAC can be described as an effective magnetic field. Therefore, in the following, we restrict our study to transverse magnetic field perturbations that induce spin mixing. This is sufficient to qualitatively understand the GSLAC PL signal due to external fields.

For the ease of generalization, we provide here the formulas to determine the effective transverse magnetic that can account for electric field and strain induced effects on the effective 2D basis of $m_S = 0$ and $m_S = -1$ states. First of all, we note that at GSLAC only certain terms of the electric field and strain coupling Hamiltonian are active due to the Zeeman splitting of the $m_S = +1$ state. These active terms are the ones that mix the $m_S = 0$ and $m_S = \pm 1$ states [38], in particular, for electric field

$$H_{E1} = d'_\perp (\{S_x, S_z\} E_x + \{S_y, S_z\} E_y), \quad (15)$$

where E_x and E_y are the x and y components of the electric field vector, respectively, and $d'_\perp$ is the NV center's electric field coupling strength whose value is expected to be of the order of 17 Hz cm/V based on recent theoretical results [38], and for strain

$$H_{\varepsilon 1} = \frac{1}{2}\left(h_{26}\varepsilon_{zx} - \frac{1}{2}h_{25}(\varepsilon_{xx} - \varepsilon_{yy})\right)\{S_x, S_z\}$$
$$+ \frac{1}{2}(h_{26}\varepsilon_{yz} + h_{25}\varepsilon_{xy})\{S_y, S_z\}, \quad (16)$$

where $h_{26} = -2830$ MHz/strain and $h_{25} = -2600$ MHz/strain are spin-strain coupling parameters [38], and $\varepsilon_{ij} = (\partial u_i/\partial x_j + \partial u_j/\partial x_i)/2$ is the strain tensor of $\vec{u}(\vec{r})$ displacement field. After reducing the 3D Hilbert space of the triplet NV center spin state to the 2D subspace of $m_S = 0$ and $m_S = -1$ states, one obtains the following formulas for the effective transverse magnetic field $b_\perp$ due to electric field

$$b_\perp = -\frac{d'_\perp}{\sqrt{2}}(E_x + E_y), \quad (17)$$

and due to strain

$$b_\perp = -\frac{1}{2\sqrt{2}}\left(h_{26}(\varepsilon_{zx} + \varepsilon_{yz}) - \frac{1}{2}h_{25}(\varepsilon_{xx} - \varepsilon_{yy} - 2\varepsilon_{xy})\right). \quad (18)$$

We study the effects of transverse magnetic field theoretically, in a spin defect-free NV center model, and experimentally, in our 99.97% ^{12}C IS diamond sample. In the simulations we evolve the density matrix according to the master equation of the closed system, Eq. (11), over 0.1 ms and calculate the average PL intensity. This procedure allows us to obtain minuscule PL features caused by weak transverse magnetic fields. In Figs. 1(b) and 1(c) the theoretical and experimental PL signals are depicted at different transverse magnetic fields. On top of the wide central dip at $B_z = 102.4$ mT, that corresponds to crossing E and to the precession of the electron spin due to the transverse field; altogether four (five) pronounced side dips can be seen on the theoretical (experimental) curves. The rightmost dip M in the experiment is related to cross relaxation with the nitrogen spin of other NV centers, for details see Sec. IV D. Side dips A, B, C, and F are well resolvable in both theory and experiment and we assign them to spin flip-flop processes induced by the transverse magnetic field. With increasing transverse field, these features shift, broaden, and change amplitude. For example, dips B and C merge with the central dip, while dip A moves away from the central dip. These features are characteristic fingerprints of external transverse fields. We note that the side dip positions are somewhat different in experiment and theory. We attribute these differences to other, unavoidable couplings in the experiment, e.g., parasitic longitudinal and transverse magnetic field, electric fields, and other spin defect.

Transverse-field dependence of the dip position, width, and amplitude can be understood through the energy level structure altered by the transverse magnetic field and the variation of the population of the states induced by additional spin flip-flop processes. As an example we discuss the case of dip C that appears at the crossing $\alpha\delta$ at 102.305 mT. In Table III we marked this crossing as not allowed, which is valid in the limit of $B_x \to 0$. Indeed, by reducing the strength of the transverse magnetic field the dip vanishes rapidly. At finite transverse field the mixing of the states at the $\beta\delta$ crossing changes the character of level δ that allows new spin flip-flop processes at $\alpha\delta$. This happens only when the transverse magnetic field is strong enough to induce overlap between the anticrossing at $\beta\delta$ and crossing at $\alpha\delta$.

Next, we discuss the magnetic field dependence of the linewidth of the central dip E at $B_z = 102.4$ mT, which is relevant for both longitudinal and transverse magnetic-field-sensing applications. We study the full width at half maximum (FWHM) for the central peak for different transverse magnetic field values both experimentally and theoretically, see Fig. 1(d). Except the region where dip C merges with the central dip, the theoretical FWHM depends linearly on the transverse field with a gradient of 3.36 mT mT^{-1}. The experimental FWHM depends also approximately linearly on the transverse magnetic field, however, at vanishing transverse magnetic field it exhibits an offset from zero. This is an indication of parasitic transverse fields and other couplings in the experiment. The slope of the experimental curve is measured
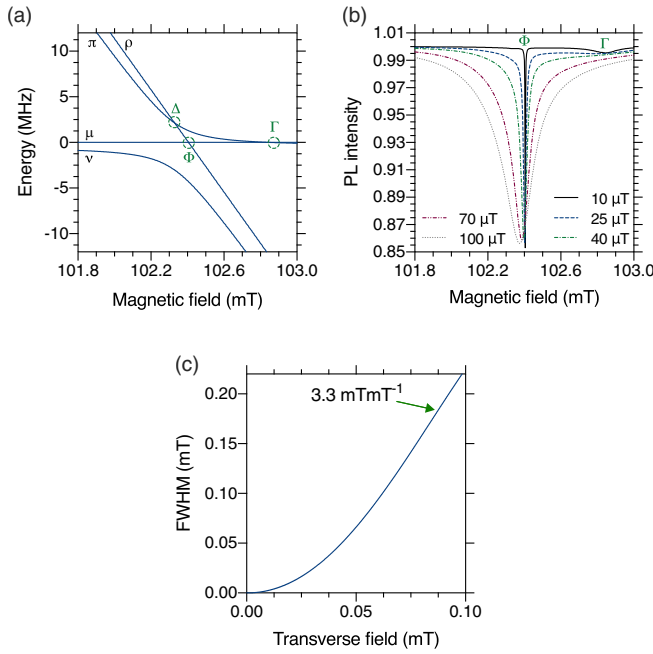
FIG. 2. (a) Energy level diagram of the ^{15}NV center. Greek letters denote the spin eigenenergies and green dashed circles with capital Greek letters denote crossings where external perturbations may open a gap. (b) Theoretical PL signal vs longitudinal magnetic field at the GSLAC with different values of transverse magnetic field. (c) Transverse magnetic field dependence of the FWHM of the pronounced dip at $\approx$102.4 mT.

to be 2.3 ± 0.1 mT mT^{-1}, which is smaller than the theoretical one. This indicates that the simulations overestimate the effect of transverse magnetic field, due to the dynamical parameters of the optical cycle, such as optical pump rate, and neglect of the shelving state that do not account for the optical excitation cycle properly. Here, we note that inhomogeneous longitudinal fields can also broaden the peaks at the GSLAC. In this case, the broadening is determined by the variance $\Delta B_\parallel$ of the longitudinal field.

Next, we theoretically investigate the PL signal of ^{15}NV center that is subject to transverse magnetic field of varying strength. The energy level structure of the two spin system is depicted in Fig. 2(a), and Table IV provides the energy eigenstates as expressed in the $|S_z, {}^{15}I_z\rangle$ basis. Besides the hyperfine interaction induced wide avoided crossing of states ν and π, three crossings can be seen in Fig. 2(a) that may give rise to PL features in the presence of transverse magnetic field.

TABLE IV. Energy eigenstates of ^{15}NV center at the GSLAC as expressed in the basis of $|S_z, I_z\rangle$, where z is parallel to the N-V axis. e and f are coefficients.

Label	Eigenstate
μ	$\|0, \uparrow\rangle$
ν	$e\|0, \downarrow\rangle + f\|-1, \uparrow\rangle$
π	$e\|-1, \uparrow\rangle + f\|0, \downarrow\rangle$
ϱ	$\|-1, \downarrow\rangle$

TABLE V. Characteristics of the level crossings at the GSLAC of the ^{15}NV center. $(\Delta S, \Delta I)$ specifies spin flip-flop processes that may take place at the crossings.

Crossing		Spin state transitions	
		$(\Delta S, \Delta I)$	Remark
Δ	$\pi\varrho$	$(\pm 1, 0)$ and $(0, \pm 1)$	electron and ^{15}N spin precession
Φ	$\mu\varrho$		no spin state transition allowed
Γ	$\mu\pi$	$(\pm 1, 0)$ and $(0, \pm 1)$	electron and ^{15}N spin precession

Figure 2(b) depicts the simulated PL signal of ^{15}NV center exhibiting two dips on the PL curves. We note that related PL signature was reported in Ref. [10], recently. Based on the position of the dips, the pronounced dip at 102.4 mT can be assigned to the crossing marked by Φ, while the shallow dip at 102.85 mT, observable only at low transverse magnetic fields, is assigned to crossing Γ. In order to describe the processes activated by the transverse magnetic field at these dips, in Table V we detail the crossings observed at the GSLAC of ^{15}NV center. As can be seen spin precession is only possible at crossing Δ and Γ and forbidden in first order at crossing Φ. Due to the high degree of polarization in state μ and the weak spin state mixing at Γ, spin precession is suppressed to a large degree at crossing Δ and Γ. The prominent PL signature at $\approx$102.4 mT is enabled by the interplay of the spin state mixing at crossing Δ and Φ. For large enough transverse magnetic fields the avoided crossing appears at Δ overlaps with the crossing at Φ that enables additional mixing with the highly polarized μ state. The role of this second order process greatly enhances as the transverse magnetic field increases and eventually gives rise to a prominent PL dip at the GSLAC.

In Fig. 2(c) we depict the transverse magnetic field dependence of the FWHM of the central dip of the GSLAC PL signal of the ^{15}NV center. Due the second-order process involved in the spin mixing, the FWHM curve is hyperboliclike. The derivative of the curve is approaching zero (3.3 mT mT^{-1}) for vanishing (large) transverse magnetic field. Due to additional perturbation and field inhomogeneities, we expect that the linewidth of the central dip saturates at a finite minimal value in experiment, similarly as we have seen for the ^{14}NV center.

The case of the ^{15}NV center demonstrates that second-order processes enabled by the perturbation of the energy level structure can also play a major role at the GSLAC. Eventually, such processes make ^{15}NV centers interesting for magnetometry applications.

B. Interaction with ^{13}C spin bath

We study the interaction of the ^{14}NV $-$ ^{13}C spin bath system at the GSLAC. We record the experimental PL spectrum in our W4 sample of natural ^{13}C abundance, in which hyperfine interaction with the surrounding nuclear spin bath is the dominant environmental interaction expectedly. A fine structure is observed that exhibits a pair of side dips at ± 48 μT distances from the central dip at 102.4 mT, see Fig. 3(a). Similar effects have been recently reported in single-NV-center measurement in Ref. [18].
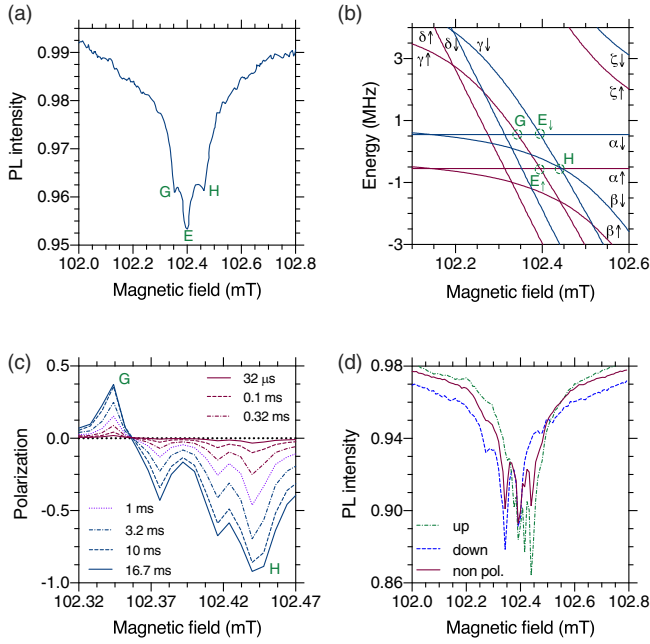
FIG. 3. PL and polarization of ^{14}NV center-^{13}C spin bath system at the GSLAC. (a) Measured PL at the GSLAC in sample W4. The PL signal indicates polarization of the ^{13}C nuclear spin bath, where the sign of the polarization is opposite at the side dips, see text for further discussion. (b) Closeup of the energy levels structure of ^{14}NV$-^{13}$C weakly coupled three spin system at the GSLAC. Greek letter with arrows specify the corresponding states, see Table II, while capital alphabet letters indicate level crossings where hyperfine interaction may give site to additional spin mixing. Maroon and blue curves depict ^{13}C nuclear spin up and down states, respectively. (c) Theoretical ensemble and site averaged polarization of a 128-spin ^{13}C spin bath obtained after optical pumping of varying duration. (d) Theoretical PL signal obtained by starting from different initial ^{13}C polarization. The solid maroon curve shows the case of initially nonpolarized spin bath, green and blue dashed lines show the PL signal obtained for initially up and down polarized spin bath, respectively. Initial polarization of the spin bath makes side dip amplitudes asymmetric.

The phenomenon can be qualitatively understood by looking at the energy-level structure of a ^{14}NV center interacting with a ^{13}C nuclear spin at the GSLAC, see Fig. 3(b), where the level labeling introduced in Fig. 1 is supplemented with either an up or down arrow depending on the spin state of the ^{13}C nucleus and the hyperfine interaction is neglected for simplicity. The central dip appears at the place of crossing $E_\downarrow$ and $E_\uparrow$, where the α and γ electron spin states of down and up ^{13}C nuclear spin projection cross, respectively. Electron spin depolarization and consequent drop of the PL intensity occur at this magnetic field due to the precession of the NV electron spin induced by the effective transverse magnetic field of the nuclear spin. The phenomenon is similar to what we have seen for the case of external transfers fields. The transverse field of the nuclear spin arises from the dipolar hyperfine coupling interaction. According to Eq. (7), the transverse field of individual nuclear spins is proportional to $\cos\theta\sin\theta$, therefore, it vanishes for $\theta = 0°$ and $90°$, while it is maximal for $\theta = 45°$ and $135°$. An important difference between external transverse field and transverse hyperfine field is that the lat-

ter varies center-to-center due to distinct local nuclear spin arrangement of individual centers. The varying traverse field induces LAC of varying width at the crossing of α and γ levels. Consequently, the central dip observed in an ensemble measurement is a superposition of numerous Lorentzian curves of varying width resulting in a typical line shape distinguishable from the line shape observed for homogeneous external fields.

The left (right) satellite dip corresponds to the crossing G (H) of states $\gamma\uparrow$ and $\alpha\downarrow$ ($\gamma\downarrow$ and $\alpha\uparrow$), where hyperfine term $S_\pm I_\mp$ ($S_\pm I_\pm$) may open a gap. According to Eq. (8), the strengths of these coupling terms are given by $A_\parallel \sin^2\theta + A_\perp(\cos^2\theta + 1)$ and $A_\parallel \sin^2\theta + A_\perp(\cos^2\theta - 1)$, respectively. Note that the terms exhibit distinct dependence on the parameters of the hyperfine tensor. Consequently, the left side dip is dominantly due to nuclear spins that are placed on the symmetry axis of the NV center, while the right side dip is dominantly due to nuclear spins that are placed next to the NV center in a plane perpendicular to the NV axis. The PL side dips are caused by mutual spin flip flops of the electron and nuclear spins that depolarize the electron spin. In turn the nuclear spins can be polarized at the magnetic field values corresponding to the side dips. Due to the different electron and nuclear spin coupling terms efficient at the different side dips, opposite nuclear spin polarization is expected. Indeed, our simulations reveal that the average nuclear polarization $P = \langle p_{+1/2} - p_{-1/2}\rangle$, where p_χ is the probability of finding individual nuclear spins in state $|\chi\rangle$, where $\chi = +1/2$ or $-1/2$, and $\langle...\rangle$ represent ensemble and bath averaging, switches as the magnetic field sweeps through the GSLAC, see Fig. 3(c). These results are in agreement with previous results [16,18].

Dynamic nuclear polarization is demonstrated in Fig. 3(c), where we depict the average nuclear spin polarization obtained after simulating continuous optical pumping of varying duration. The pumping rate is set to 333 kHz in the simulations. It is apparent from the figure that the average nuclear polarization continuously increases as the pumping period extends. The positive and the largest negative polarization dip correspond to the crossing G and H, respectively. The complicated pattern is, however, the result of the interplay of different processes that take place at other, not labeled crossings. It is also apparent from the figures that DNP is considerably stronger at the magnetic field corresponding to the right dip. We also note that in the simulations considerable finite-size effects are observed due to the limited number of spins included in the model, see Appendix. Therefore, quantitative results reported in Fig. 3(c) are not representative to the bulk but rather to nanodiamond samples of ≈ 5 nm size embedding a single, magnetic field aligned NV center. In such small nanoparticles nuclear spin diffusion may be negligible, as it is in the simulations.

As the NV center has an effect on the nuclear polarization, the nuclear polarization has also an effect on the NV center, especially on the PL signature at the GSLAC. Similar effects were also seen in single NV center measurements [18]. Polarization of the nuclear spins populates and depopulates certain levels that makes the effects of certain level crossing more or less pronounced. In Fig. 3(d) we model the GSLAC PL spectrum of NV centers interacting with polarized and

nonpolarized spin baths. Note that the simulation time is set only to 32 μs in order not to alter the initial polarization significantly. Polarization in nuclear spin up (down) state completely reduces the left (right) dip but in turn enhances the right (left) dip amplitude. Furthermore, an additional shallower satellite dips appears. In contrast, the central dip amplitude is affected only marginally by the degree and sign of the nuclear spin polarization. When the spin bath is not polarized initially, i.e., it only polarizes due to optical pumping according to Fig. 3(c), we observe two side dips of similar amplitudes in the simulations.

The theoretical PL curve of nonpolarized ^{13}C spin bath in Fig. 3(d) resembles the experimental curve Fig. 3(a), however, the amplitude of the side dips is overestimated. As we have seen, this amplitude depends considerably on the polarization of the bath. The relatively small side dip amplitudes in the experiment indicate considerable polarization. We note that the numerical simulation cannot reproduce these curves completely due to finite-size effects observed in the simulations. As mentioned above, DNP at the higher-magnetic-field side dip, that polarizes in the perpendicular plane, is more efficient. Therefore, polarization reaches the side of the simulation box quickly in the simulation, after which the nuclear polarization increases rapidly and reduces the right side dip that makes the PL side dips asymmetric in amplitude, see Appendix. To circumvent this issue, one may utilize a model including ^{13}C nuclear spins in a larger, disk shaped volume centered at the NV center.

Next, we theoretically investigate the PL spectrum of the ^{15}NV $-\,^{13}$C system. The simulated GSLAC PL spectrum, depicted in Fig. 4(a), reveals a multidip fine structure with four distinct dips labeled by capital Greek letters. While the central dip Φ and its satellite dip Θ are less prominent compared to the central dip of the ^{14}NV GSLAC PL signal, we observe two major side dips at larger distances. These dips are similar in amplitude and nearly symmetrical to the central dip, however, their origin is completely different. Figure 4(b) depicts the energy-level structure of the ^{15}NV $-\,^{13}$C system and identifies the level crossings that are responsible for the observed dips. The central dip and the satellite dip Θ correspond to the precession of the electron spin driven by the effective transverse field of the ^{13}C nuclear spin bath. Side dip Λ appears at the crossing of states of different ^{13}C magnetic quantum number, thus hyperfine flip-flop operators may induce mixing between the nuclear and electron spin states. At the place of the dip Λ, DNP may be realized. Finally, side dip Ω appears at the crossing of levels of identical ^{13}C nuclear spin quantum numbers suggesting that here electron spin precession plays a major role.

Figures 4(c) and 4(d) depict the polarization of the ^{15}N nuclear spin and the site and ensemble averaged polarization of the ^{13}C nuclear spins, respectively. Polarization of ^{15}N nuclear spin closely follows polarization of the electron spin due to their strong coupling. In absolute terms, the depolarization of the ^{15}N nuclear spin is twice as large as the electron spin's depolarization indicating that ^{15}N nuclear spin plays a role in forming the PL dips. The average polarization of the ^{13}C spin bath shows distinct signatures, see Fig. 4(d). Efficient polarization transfer is only possible at the magnetic field corresponding to dip Λ, where electron spin-nuclear spin mixing
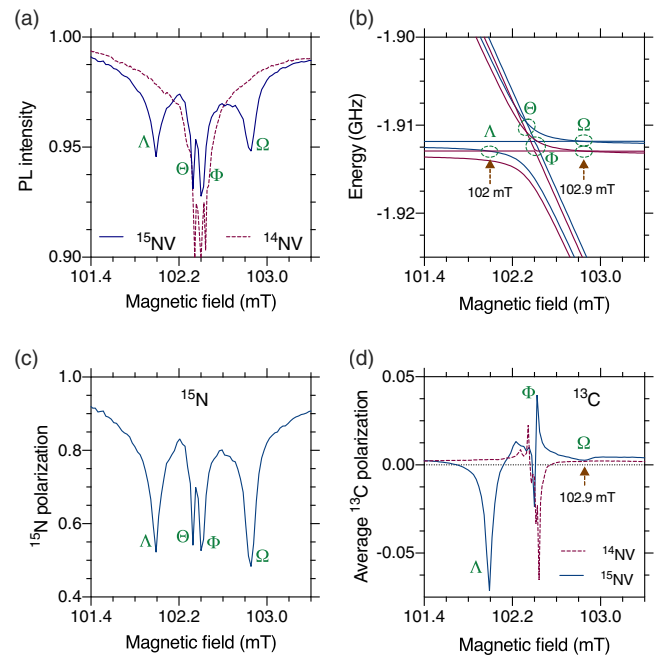

FIG. 4. PL and polarization of ^{15}NV center-^{13}C spin bath system at the GSLAC. (a) PL spectrum of ^{15}NV $-\,^{13}$C system (solid blue curve) as compared to the PL spectrum of the ^{14}NV $-\,^{13}$C system (dashed maroon curve). (b) Energy-level structure at the GSLAC. Blue and maroon curves correspond to $|-1/2\rangle$ and $|+1/2\rangle$ nuclear spin states, respectively. Relevant crossings of the energy levels are indicated with green dashed circles and labeled by capital letters. (c) and (d) depict the polarization of ^{15}N nuclear spin and ensemble and site averaged polarization of ^{13}C nuclear spin bath, respectively. For comparison ^{13}C nuclear spin bath polarization induced by a ^{14}NV center at the GSLAC is also depicted in (d).

is possible. At the central dip Φ spin coupling gives rise to a sharp alternating polarization pattern. At dip Θ and Ω we observe only shallow dips in the ^{13}C polarization. In order to compare ^{14}NV and ^{15}NV DNP processes we depicted in Fig. 4(d) the averaged nuclear spin polarization obtained for ^{14}NV center as well. After a fixed 0.3 ms optical pumping, we see that nuclear spin polarization achieved in the two cases is comparable.

As can be seen in Fig. 4(d) polarization transfer can be as efficient as for the ^{14}NV center. The fact that the crossing states at dip Λ contain only slight contribution from the $|m_S = -1\rangle$ electron spin state suggests that the polarization transfer is suppressed. In contrast, we obtain considerable polarization that we attribute to the absence of competing flip-flop processes at dip Λ. Processes that could hinder polarization transfer, such as electron spin precession at dip Θ and Φ, are well separated, in contrast to the case of ^{14}NV center. These results indicate that besides the most often considered ^{14}NV center, the ^{15}NV center system may also be utilized in MW free DNP applications.

C. Interaction with P1 center and other spin-1/2 point defects

Diamond often hosts paramagnetic point defects that can interact with the NV centers at the GSLAC. The spin-1/2 P1
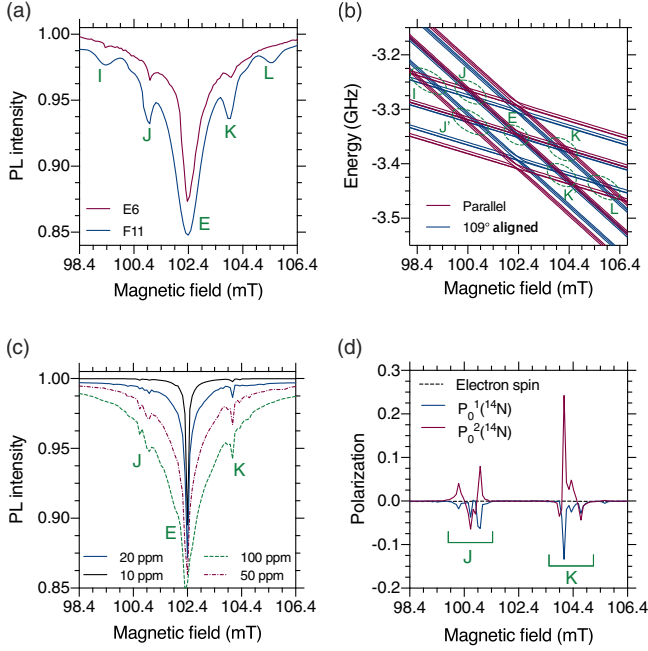
FIG. 5. Interaction with P1 centers at the GSLAC. (a) Experimental PL spectrum recorded in two samples of different P1 concentration, see Table I. PL intensities were scaled to be comparable with each other. (b) Energy-level structure of P1 centers. Maroon and blue curves show the case of magnetic field aligned and 109° aligned P1 centers, respectively. (c) Theoretical PL spectrum for different P1 center concentrations. (d) Ensemble and site averaged electron and ^{14}N nuclear spin polarization of the P1 center.

center is a dominant defect in diamond. This defect does not exhibit level crossing at the magnetic field corresponding to the GSLAC, see Sec. II. Due to the large energy gap between the electron spin states, the central NV center couples nonresonantly to P1 center. This limits the range of interactions to some extent, however, as we show below, efficient coupling is still possible.

We study the PL signature of two different samples, E6 and F11, that contain P1 centers in 13.8 ppm and 100–200 ppm concentrations, respectively, see Fig. 5(a). Depending on the P1 concentration, we observe either three or five dips in the PL intensity curve. A similar signal has been reported recently in Refs. [20–22]. In sample F11 of higher P1 center concentration, two pairs of side dips, I and L and J and K, can be seen around the central dip E at 102.4 mT. In sample E6 of lower P1 center concentration only side dips J and K can be resolved beside the central dip. Note that the distance of the side dips from the central dip is an order of magnitude larger than in the case of ^{13}C spin environment, thus these signatures are not related to the nuclear spin bath around the NV center.

In Fig. 5(b) we depict the energy-level structure of the magnetic field aligned and 109° aligned P1 centers for $m_{P1} = -1/2$, where one can see three groups of lines for both $m_S = 0$ and $m_S = -1$. These separate groups of lines can be assigned to the different quantum numbers of the ^{14}N nuclear spin of the P1 center. The corresponding states split due to the strong hyperfine interaction. Note that similar energy level structure can be seen for $m_{P1} = +1/2$ at 2.8 GHz higher energy. From

the comparison of the place of the crossings and the dips in the PL signature we can assign each of the dips to separate crossing regions. The central crossing, labeled E, where the crossing states possess identical P1 center electron and ^{14}N nuclear spin projection quantum numbers, is responsible for the central dip. Similarly to the case of the ^{13}C nuclear spin, the NV electron spin precesses in the effective transverse field of the P1 center caused by the nonsecular $S_\pm S_z^{P1}$ term of the dipole-dipole interaction. Side dips J and K (I and L) correspond to crossings where the quantum number of the nuclear spin of the P1 center changes by ±1 (±2). In recent nanoscale relaxation time magnetic resonance (T$_1$-MR) spectroscopy measurements P1 center related signals were recorded at magnetic field values corresponding to side peak J and K [39].

Next, we theoretically study the PL signal of NV centers interacting with P1 centers ensembles of different concentration, see Fig. 5(c). As one can see, the theoretical curves resemble the experimental ones, however, there are important differences. Even in large P1 concentrations we only see side dips J and K besides dip E in the simulations. The amplitude of the side dips is also underestimated. Furthermore, the shape of the central peak is different in the simulations and in the experiment, especially in sample E6. The latter can be described by a Lorentzian curve, similarly as we have seen for external fields. This may indicate considerable transverse magnetic field or strain in sample E6.

To further study the mechanism responsible for the side dips, we study the magnetic field dependence of the polarization of the electron spin and the ^{14}N nuclear spin of the P1 center. The latter can be characterized by ϱ_0^0 monopole, ϱ_0^1 dipole, and ϱ_0^2 quadrupole moments that correspond to population, orientation, and alignment, respectively [23]. Orientation and alignment can be obtained from quantities p_m defining the probability of finding the nuclear spin in state $|m\rangle$ as

$$P_0^1 = \frac{\varrho_0^1}{\varrho_0^0} = \sqrt{\frac{3}{2}} \frac{p_1 - p_{-1}}{p_1 + p_0 + p_{-1}} \tag{19}$$

and

$$P_0^2 = \frac{\varrho_0^2}{\varrho_0^0} = \sqrt{\frac{1}{2}} \frac{p_1 + p_{-1} - 2p_0}{p_1 + p_0 + p_{-1}}, \tag{20}$$

respectively. The polarization curves as a function of the external magnetic field are depicted in Fig. 5(d). Note that the electron spin does not exhibit any polarization. This is due to the fact that the large, 2.8 GHz splitting of the P1 center electron spin states at the GSLAC suppresses flip-flop processes that could polarize the P1 center. The nuclear spin polarization observed in Fig. 5(d) might be unexpected, as the electron spin of the P1 center cannot polarize the nuclear spin. Instead, the NV center directly polarizes the nuclear spin of the P1 center. This direct interaction is made possible by the hyperfine coupling that mixes the electron and nuclear spin of the P1 center. Considering only the nuclear spin states, the hyperfine mixing gives rise to an effective g factor that may be significantly enhanced due to the contribution of the electron spin. This finding supports previous explanations [39]. It is apparent from Fig. 5(d) that the nuclear polarization exhibits

a fine structure at the magnetic fields that correspond to side dips J and K. This fine structure cannot be resolved in the experimental PL spectrum, however, clearly visible in T_1-MR measurement in Ref. [39].

As side dips I and L do not appear in the theoretical simulation we can only provide tentative explanation of these dips. The positions of the dips correspond to magnetic fields where the crossings are related to P1 center nuclear spin state $|+1\rangle$ and $|-1\rangle$. Therefore, to flip the NV electron spin, the quantum number of the P1 center nuclear spin must change by 2. This may be allowed by the interplay of other spins. For example, ^{13}C nuclear spin around the NV center or P1 center-P1 center interaction may contribute to this process. As side dips I and L are pronounced only at higher P1 center concentrations, we anticipate that the second process is more relevant.

Next, we investigate the linewidth of the central dip E. The varying local environment of the NV centers can induce magnetic field inhomogeneity in an ensemble that broadens the central GSLAC PL dip. This effect may limit the sensitivity of magnetic field sensors. The FWHM for varying P1 concentration c, ranging from 10 ppm to 200 ppm, is considered. By fitting a linear curve to the theoretical points we obtain a slope of ≈ 20 μT/ppm.

Finally, we note that the example of P1 center can be easily generalized to the case of other spin-1/2 point defects. Through the effective transverse magnetic field of the defects, one may expect contribution to the central dip at 102.4 mT. Furthermore, depending on the hyperfine interactions at the paramagnetic defect site, one may observe side dips placed symmetrically beside the central dip. When the point defect includes a paramagnetic isotope of high natural abundance that couples strongly to the electron spin, a pronounced PL signature may be observed at the GSLAC.

The example of P1 center demonstrates that nuclear spins around spin-1/2 defects can be polarized by the NV center. This phenomena may enable novel DNP applications at the GSLAC. Furthermore, we demonstrated both experimentally and theoretically that GSLAC PL signature depends on the concentration of the spin defect in the vicinity of the NV centers. This realization may motivate the use of GSLAC PL signal in spin defect concentration measurements.

D. NV spin bath

Next, we investigate the case of ^{14}NV center coupled to magnetic-field-aligned ^{14}NV centers. Note that in this case both the central spin and the bath spins exhibit crossings and anticrossings at the GSLAC. The simulated PL spectrum is depicted in Fig. 6(a) for various spin-bath concentrations. As can be seen, two dominant dips, E and M, are observed with additional shoulders appearing at higher concentrations. To track down the origin of the most visible dips, we depict energy curves of allowed $|m_S, m_{I_{14N}}\rangle \rightarrow |m'_S, m'_{I_{14N}}\rangle$ spin-state transitions of an individual NV center in Fig. 6(b). Transition-energy curves are differences of energy levels that we label by pairs of Greek letters $\mu\nu$, where μ and ν represent levels of individual NV centers, see Fig. 1 and Table II. Crossings in the energy level structure of an individual NV center are represented in the transition energy plot by curves approaching zero
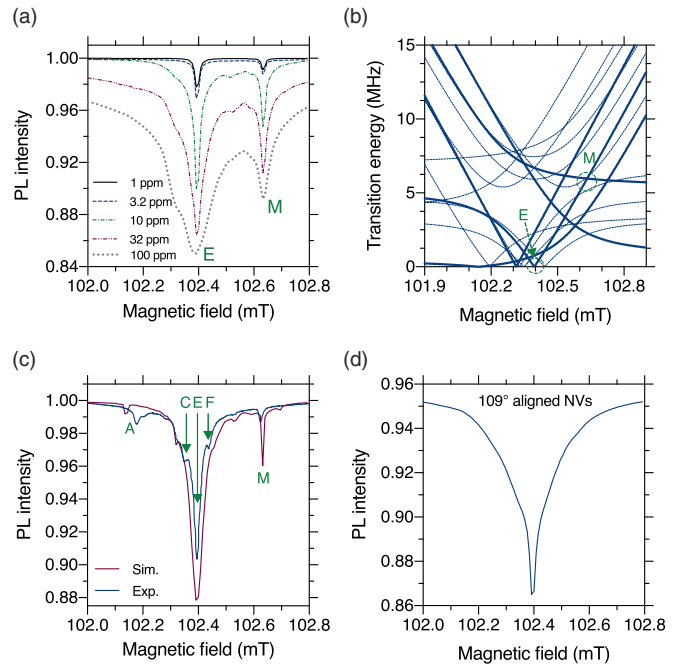

FIG. 6. Photoluminescence of ^{14}NV center-^{14}NV center spin-bath system at the GSLAC. (a) Simulated PL spectrum of ^{14}NV center-magnetic field aligned ^{14}NV spin-bath system at different concentrations ranging from 1 ppm to 100 ppm. (b) Transition energy curves, see text for clarification, at the GSLAC. Wide solid curves highlight transitions associated to the highest populated α state of individual NV centers. Dashed curves show transition energies associated to transitions between less populated energy levels. Green dashed circle labeled by A mark the place of level crossing where the central NV center precesses in the transverse field of other NV centers. Crossing B between the transition energy curves represents a place of effective cross relaxation between the NV centers that gives rise to dip B in the PL scan. (c) Experimental GSLAC PL spectrum obtained in our IS diamond sample as compared with simulation of 0.5 ppm field oriented NV center spin bath and 15 μT transverse magnetic field. Signatures of both the transverse field and the parallel NV centers are visible on the experimental and theoretical curves. (d) Simulated PL spectrum with 109° aligned NV center spin bath.

at the places of the level crossings. Crossing of the transition energy curves at nonzero energy means that certain spin state transitions have the same energy. Furthermore, cross relaxation between two NV centers can occur when their transition energies are resonant. Due to the identical level structure of the central NV center and the coupled NV centers, crossings of transition energy curves in Fig. 6(b) represent places of efficient cross relaxation between aligned NV centers. Cross relaxation can induce depolarization of the central spin that may give rise to dips in the PL spectrum. There are numerous cross relaxation places that can be identified in Fig. 6(b). Most of them, however, are not active due to the high polarization of the coupled NV centers. Relevant transition-energy curves associated to the highest populated energy level α in Fig. 1 are highlighted in Fig. 6(b) by wide solid lines. Dip E appears at the magnetic field where $\alpha\gamma$ transition energy vanishes, i.e., α and γ states cross, enabling precession of the central NV center in the transverse field of other NV centers, similarly as

we have seen for ^{13}C and P1-center spin baths. We assign the source of dip M in the PL spectrum to a crossing between $\alpha\gamma$ and $\alpha\varepsilon$ transition energy curves. At the magnetic field of the transition-energy crossing $\alpha\gamma$ transition corresponds dominantly to $|0, +1\rangle \leftrightarrow |-1, +1\rangle$ transition, while $\alpha\varepsilon$ transition corresponds dominantly to $|0, +1\rangle \leftrightarrow |0, 0\rangle$ transition. Therefore, at dip M efficient cross relaxation between the electron and the nuclear spins of the two centers takes place.

To demonstrate ^{14}NV – ^{14}NV couplings at the GSLAC experimentally we carry out PL measurement in our IS sample. In Fig. 6(c) one can see the experimental PL spectrum obtained at near perfect alignment of the external magnetic field and the NV axis. The residual transverse field is estimated to be $\approx$3.6 μT. The experimental curve exhibits several dips. To identify each of them we carried out theoretical simulations including additional external transverse magnetic fields of 15 μT strength. External field is applied solely to the central spin to mimic local transverse inhomogeneities. It is apparent from the comparison that the experimental curve exhibits the signatures of both local field inhomogeneities and interaction with field aligned NV centers in our ^{13}C depleted sample.

Finally, in Fig. 6(d), we theoretically investigate the effect of 109° aligned NV center of 10 ppm concentration. These spin defects act like a source of local inhomogeneous transverse field that gives rise to PL signature similar to the central dip of P1 center induced spin bath. The FWHM of the curve is however twice larger than the FWHM of the P1 center induced PL signature at the same concentration. This is due to the larger magnetic moment of the NV center.

V. SUMMARY AND DISCUSSION

The ground-state avoided crossing of the NV center spin states gives rise to a variety of couplings that imply different behavior of the NV center. In our study we considered the most relevant couplings and demonstrated that each of them gives rise to a unique PL signature that enables identification of the dominant environmental couplings in a given sample. This may be informative for optimizing defect concentration in samples and experimental setups.

At the GSLAC, gapless electron spin states mix with the states of numerous quantum objects. In such circumstances entanglement may built up between different parts of the many-body system. This nonclassical correlation may affect the dynamics of the system and can have both positive and negative effect on the spin transport between the central NV center and other coupled quantum objects. Our theoretical approach is able to systematically include nonclassical correlation effects. We studied the effect of n-spin entanglement, see the Appendix, where n goes up to 6, on the PL signal of the NV center at the GSLAC in the most critical case, where the NV center couples to a nuclear spin bath of long-lived quantum states. Our simulations demonstrate the presence of destructive interference in the nuclear spin bath dynamics that negatively affects spin transport and give rise to reduction of the PL signal intensity, see Fig. 7(a) in the Appendix.

We introduce that any time independent external field can be expressed as an effective magnetic field at the GSLAC. This mathematically rigorous statement allows one to generalize our transverse magnetic field dependence study to strain
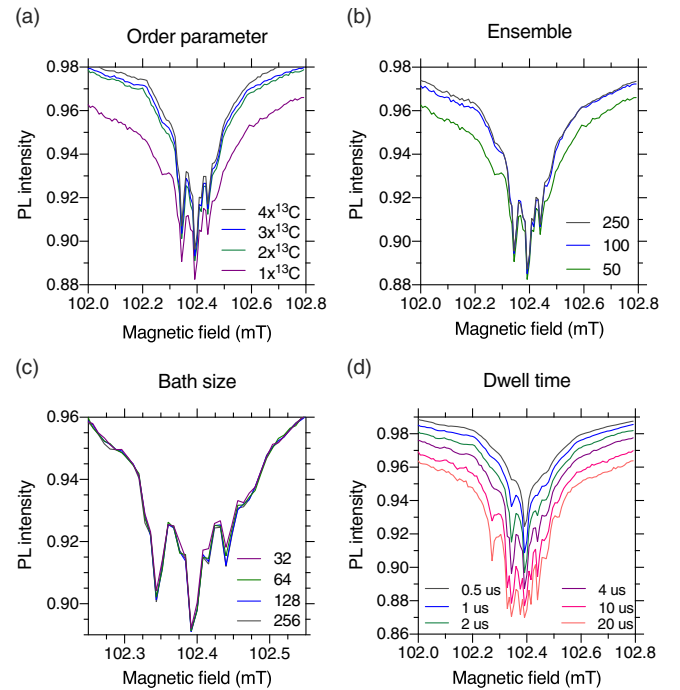

FIG. 7. Optimization of the simulation parameters. (a), (b), (c), and (d) show the GSLAC PL signal of ^{14}NV – ^{13}C system for different order parameter, ensemble size, bath size, and ground-state dwell time, respectively.

and electric field. Using the formulas provided in Eqs. (17) and (18) the results depicted in Fig. 1 can be straightforwardly generalized to any static external field and strain.

Details of the spin transport between ^{13}C spin bath and ^{14}NV and ^{15}NV centers are studied using realistic hyperfine coupling tensors obtained from *ab initio* DFT calculations and higher level modeling. Our findings demonstrate that not only ^{14}NV center but also ^{15}NV can be utilized in hyperpolarization experiment with comparable polarization transport ability.

We demonstrated that, despite the suppressed coupling of the P1 center and NV center electron spins, nuclear spins coupled to a P1 center can be polarized by the NV center at the GSLAC through an effective hyperfine interaction greatly enhanced by the electron spin-electron spin coupling and the hyperfine interaction at the P1 center site. This coupling opens new directions for DNP applications through P1 centers and other spin-1/2 defects at the GSLAC. For example, farther nuclear spin ensembles can be polarized by the NV center without relying on nuclear spin diffusion. This possibility may be particularly important for near surface NV centers that may polarize nuclear spins at the surface though paramagnetic surface defects. In addition, we demonstrated that the GSLAC PL signal depends considerably on the concentration of paramagnetic point defects, therefore it may serve as a tool for measuring spin defect concentration in the vicinity of NV centers.

Finally, we demonstrated that mutually aligned NV centers can also couple at the GSLAC opening alternatives for gate operations. While the energy-level structure of coupled NV centers is quite involved at the GSLAC, different spin flip-flop processes resonantly enhance at certain magnetic fields.

Depending on the states and the magnetic field, all sorts of operations are possible. We note that ^{15}NV centers are of great potential in this respect as well. Due to the larger hyperfine splitting and the reduced number of states crossing at the GSLAC, the ^{15}NV centers may be better controllable.

APPENDIX A: CONVERGENCE TESTS

In order to determine the optimal simulation settings, we carry out initial convergence tests. We consider ^{13}C spin bath, that may couple coherently to the central NV center, due to the long coherence time of the nuclear spins and the relatively strong coupling strength for the closest nuclear spins.

Neglect of spin-bath correlation effects is the main approximation of the utilized theoretical approach. Spin-bath correlation can be included systematically in the simulations, however, by increasing the order of cluster approximation, i.e., the number of spins included in each subsystem. In Fig. 7(a), we depict the PL signal obtained for different order parameters, where one can see a significant difference between the case of noncorrelated spin bath, $1 \times ^{13}$C, and partially correlated cases, $N \times ^{13}$C, where $N > 1$. Beyond
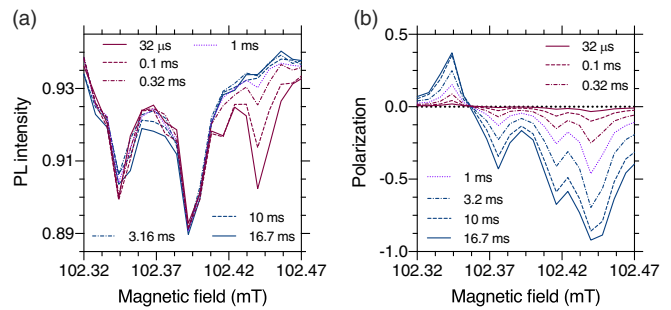

FIG. 8. (a) PL signal and (b) ^{13}C polarization after varying length of optical pumping of a ^{14}NV center at the GSLAC.

$N = 2$, the PL curves change only slightly, thus we use $N = 2$ in the simulations of ^{13}C spin bath. Note that other spin defects considered in the main text include electron spins that usually possess much shorter coherence time, therefore the bath may be considered uncorrelated and the first-order cluster approximation is appropriate in those cases.

In Figs. 7(b) and 7(c), we study ensemble- and bath-size dependence of the GSLAC PL signal. As can be seen 100 and 128 are convergent settings for the ensemble and bath sizes, respectively. Finally, in Fig. 7(d), we investigate ground-state dwell-time dependence of the PL curves. For increasing dwell time we observe additional fine structures appearing. In the simulations we use 3 μs dwell time that is a reasonable choice knowing the optical laser power usually used in the experiments.

APPENDIX B: PUMPING-DURATION DEPENDENCE OF THE GSLAC PL SIGNAL AND THE ^{13}C NUCLEAR POLARIZATION

In Figs. 8(a) and 8(b) we depict the GSLAC PL signature and the average nuclear polarization of a ^{13}C bath as obtained after varying length of optical pumping of a ^{14}NV center. Averaging is carried out over an ensemble of 100 randomly generated NV center-^{13}C spin bath configurations, each of which includes 127 ^{13}C nuclear spins in an arrangement corresponding to natural abundance. With increasing time the right PL side dip reduces rapidly, while the left side dip reduces only moderately in the simulations. The corresponding rightmost and leftmost nuclear polarization peaks in Fig. 8(b) grows rapidly and modestly, respectively. This shows that the polarization transfer is most efficient at the magnetic field corresponding to the right PL side dip. As the efficiency of the polarization transfer is varying at the left and right dips, finite-size effects influence the side dips differently. The different pumping duration dependence of the PL side-dip amplitudes observed in Fig. 8(a) is attributed to this effect.

[1] L. du Preez, Ph.D. thesis, University of Witwatersrand, 1965.

[2] J. Wrachtrup and F. Jelezko, J. Phys.: Condens. Matter **18**, S807 (2006).

[3] J. R. Maze, A. Gali, E. Togan, Y. Chu, A. Trifonov, E. Kaxiras, and M. D. Lukin, New J. Phys. **13**, 025025 (2011).

[4] M. W. Doherty, N. B. Manson, P. Delaney, F. Jelezko, J. Wrachtrup, and L. C. Hollenberg, Phys. Rep. **528**, 1 (2013).

[5] J. R. Maze, P. L. Stanwix, J. S. Hodges, S. Hong, J. M. Taylor, P. Cappellaro, L. Jiang, M. V. G. Dutt, E. Togan, A. S. Zibrov,

A. Yacoby, R. L. Walsworth, and M. D. Lukin, Nature (London) **455**, 644 (2008).

[6] G. Balasubramanian, P. Neumann, D. Twitchen, M. Markham, R. Kolesov, N. Mizuochi, J. Isoya, J. Achard, J. Beck, J. Tissler, V. Jacques, P. R. Hemmer, F. Jelezko, and J. Wrachtrup, Nat. Mater. **8**, 383 (2009).

[7] F. Dolde, H. Fedder, M. W. Doherty, T. Nöbauer, F. Rempp, G. Balasubramanian, T. Wolf, F. Reinhard, L. C. L. Hollenberg, F. Jelezko, and J. Wrachtrup, Nat. Phys. **7**, 459 (2011).

[8] G. Kucsko, P. C. Maurer, N. Y. Yao, M. Kubo, H. J. Noh, P. K. Lo, H. Park, and M. D. Lukin, Nature (London) **500**, 54 (2013).

[9] J. Teissier, A. Barfuss, P. Appel, E. Neu, and P. Maletinsky, Phys. Rev. Lett. **113**, 020503 (2014).

[10] D. A. Broadway, J. D. A. Wood, L. T. Hall, A. Stacey, M. Markham, D. A. Simpson, J.-P. Tetienne, and L. C. L. Hollenberg, Phys. Rev. Appl. **6**, 064001 (2016).

[11] A. Wickenbrock, H. Zheng, L. Bougas, N. Leefer, S. Afach, A. Jarmola, V. M. Acosta, and D. Budker, Appl. Phys. Lett. **109**, 053505 (2016).

[12] H. Zheng, Z. Sun, G. Chatzidrosos, C. Zhang, K. Nakamura, H. Sumiya, T. Ohshima, J. Isoya, J. Wrachtrup, A. Wickenbrock, and D. Budker, Phys. Rev. Appl. **13**, 044023 (2020).

[13] R. J. Epstein, F. M. Mendoza, Y. K. Kato, and D. D. Awschalom, Nat. Phys. **1**, 94 (2005).

[14] H.-J. Wang, C. S. Shin, S. J. Seltzer, C. E. Avalos, A. Pines, and V. S. Bajaj, Nat. Commun. **5**, 4135 (2014).

[15] J. D. A. Wood, J.-P. Tetienne, D. A. Broadway, L. T. Hall, D. A. Simpson, A. Stacey, and L. C. L. Hollenberg, Nat. Commun. **8**, 15950 (2017).

[16] H.-J. Wang, C. S. Shin, C. E. Avalos, S. J. Seltzer, D. Budker, A. Pines, and V. S. Bajaj, Nat. Commun. **4**, 1940 (2013).

[17] V. Ivády, P. V. Klimov, K. C. Miao, A. L. Falk, D. J. Christle, K. Szász, I. A. Abrikosov, D. D. Awschalom, and A. Gali, Phys. Rev. Lett. **117**, 220503 (2016).

[18] D. A. Broadway, J.-P. Tetienne, A. Stacey, J. D. A. Wood, D. A. Simpson, L. T. Hall, and L. C. L. Hollenberg, Nat. Commun. **9**, 1246 (2018).

[19] K. Holliday, N. B. Manson, M. Glasbeek, and E. van Oort, J. Phys.: Condens. Matter **1**, 7093 (1989).

[20] S. Armstrong, L. J. Rogers, R. L. McMurtrie, and N. B. Manson, Phys. Procedia **3**, 1569 (2010), proceedings of the Tenth International Meeting on Hole Burning, Single Molecule and Related Spectroscopies: Science and Applications-HBSM 2009.

[21] S. V. Anishchik and K. L. Ivanov, Phys. Rev. B **96**, 115142 (2017).

[22] S. Anishchik and K. Ivanov, J. Magn. Reson. **305**, 67 (2019).

[23] M. Auzinsh, A. Berzins, D. Budker, L. Busaite, R. Ferber, F. Gahbauer, R. Lazda, A. Wickenbrock, and H. Zheng, Phys. Rev. B **100**, 075204 (2019).

[24] H. Clevenson, E. H. Chen, F. Dolde, C. Teale, D. Englund, and D. Braje, Phys. Rev. A **94**, 021401(R) (2016).

[25] A. K. Dmitriev, H. Y. Chen, G. D. Fuchs, and A. K. Vershovskii, Phys. Rev. A **100**, 011801(R) (2019).

[26] V. Jacques, P. Neumann, J. Beck, M. Markham, D. Twitchen, J. Meijer, F. Kaiser, G. Balasubramanian, F. Jelezko, and J. Wrachtrup, Phys. Rev. Lett. **102**, 057403 (2009).

[27] V. Ivády, K. Szász, A. L. Falk, P. V. Klimov, D. J. Christle, E. Janzén, I. A. Abrikosov, D. D. Awschalom, and A. Gali, Phys. Rev. B **92**, 115206 (2015).

[28] D. V. Sosnovsky and K. L. Ivanov, Mol. Phys. **117**, 2740 (2019).

[29] P. Fernández-Acebal, O. Rosolio, J. Scheuer, C. Müller, S. Müller, S. Schmitt, L. McGuinness, I. Schwarz, Q. Chen, A. Retzker, B. Naydenov, F. Jelezko, and M. Plenio, Nano Lett. **18**, 1882 (2018).

[30] A. Ajoy, K. Liu, R. Nazaryan, X. Lv, P. R. Zangara, B. Safvati, G. Wang, D. Arnold, G. Li, A. Lin, P. Raghavan, E. Druga, S. Dhomkar, D. Pagliero, J. A. Reimer, D. Suter, C. A. Meriles, and A. Pines, Sci. Adv. **4**, eaar5492 (2018).

[31] I. Schwartz, J. Scheuer, B. Tratzmiller, S. Müller, Q. Chen, I. Dhand, Z.-Y. Wang, C. Müller, B. Naydenov, F. Jelezko, and M. B. Plenio, Sci. Adv. **4**, eaat8978 (2018).

[32] F. Shagieva, S. Zaiser, P. Neumann, D. B. R. Dasari, R. Stöhr, A. Denisenko, R. Reuter, C. A. Meriles, and J. Wrachtrup, Nano Lett. **18**, 3731 (2018).

[33] P. R. Zangara, J. Henshaw, D. Pagliero, A. Ajoy, J. A. Reimer, A. Pines, and C. A. Meriles, Nano Lett. **19**, 2389 (2019).

[34] V. Ivády, Phys. Rev. B **101**, 155203 (2020).

[35] S. Felton, A. M. Edmonds, M. E. Newton, P. M. Martineau, D. Fisher, D. J. Twitchen, and J. M. Baker, Phys. Rev. B **79**, 075203 (2009).

[36] R. J. Cook and D. H. Whiffen, Proc. R. Soc. Lond. A **295**, 99 (1966).

[37] K. Szász, T. Hornos, M. Marsman, and A. Gali, Phys. Rev. B **88**, 075202 (2013).

[38] P. Udvarhelyi, V. O. Shkolnikov, A. Gali, G. Burkard, and A. Pályi, Phys. Rev. B **98**, 075201 (2018).

[39] J. D. A. Wood, D. A. Broadway, L. T. Hall, A. Stacey, D. A. Simpson, J.-P. Tetienne, and L. C. L. Hollenberg, Phys. Rev. B **94**, 155402 (2016).

Correction: The "Corresponding author" identifiers were missing at publication and have now been inserted.